

AIAA - 2001 - 3073

**SIMULATION OF COMPRESSIBLE GAS
FLOW IN A MICRONOZZLE**
Effect of Walls on Shock Structure

By

M. Buoni, D. Dietz, K. Aslam, and V. V. Subramaniam

**Center for Advanced Plasma Engineering
Non-Equilibrium Thermodynamics Laboratories
Department of Mechanical Engineering
The Ohio State University
Columbus, Ohio 43210, U.S.A.**

**35th AIAA Thermophysics
Conference**
11-14 June 2001/Anaheim, CA

Abstract

High-speed, compressible flow of Argon through a converging-diverging micronozzle is examined using the Direct Simulation Monte Carlo (DSMC) method in this paper. The upstream and downstream conditions are chosen so as to yield Knudsen numbers (either based on the constant transverse dimension of the throat or on the local transverse dimension of the micronozzle) in the transition regime. The structure of a shock wave in the transition regime in a micronozzle is examined for a total pressure $P_o \sim 1$ Torr, total temperature $T_o = 298$ K, and exit pressure $P_{\text{exit}} = 0.2$ Torr, for the two limiting cases of diffuse walls (no-slip) and specular walls (maximum slip). DSMC results indicate that for these conditions, there is a discernible shock in the diverging portion of the micronozzle in the case of specular walls, reminiscent of shocks in continuum internal flows, while a spread-out shock occupies much of the diverging portion in the case of diffuse walls. The fact that wall-interactions can influence the flow-field and shock structure in such a dramatic fashion presents an opportunity to tailor the performance of micronozzles either through the use of novel coatings or by choice of micronozzle material, for a given gas.

I. Introduction

Modern silicon-based semiconductor technology has enabled use of its many etching and growth processes for fabrication at small scales. These fabrication techniques have been used to develop Micro Electro-Mechanical Systems or MEMS and various micro-devices. Among the many MEMS devices are low-thrust micronozzles, which may be useful individually or in an array for propulsion of small satellites. Of particular interest are micronozzles operating under conditions where the local mean free path ($\bar{\lambda}$) is on the order of the characteristic nozzle dimension (such as throat diameter, d , for example). When nozzles are operated, transients inevitably ensue during start-up or shut-down, until a steady state is reached. During these transients, it is not uncommon to find normal shock waves, oblique shock waves, and expansion fans inside the nozzle. In this work, we focus on a numerical study of the structure of shock waves in a micronozzle that is operated in the transition regime. Of particular interest are viscous effects and the

role of bounding walls in such compressible, internal flows with shocks.

The Reynolds number, $Re = \frac{Vy_t}{\nu}$,

where V is a characteristic velocity, ν is the kinematic viscosity, and y_t is the transverse dimension of the throat (y_t is the throat diameter for an axi-symmetric geometry), is typically small for micronozzle flows. Since ν scales as the mean free path, it can be seen that Re scales as the ratio of the characteristic length (transverse dimension of the throat) to the mean free path. At lower nozzle operating pressures, this ratio ($y_t / \bar{\lambda}$) decreases, resulting in low Reynolds numbers corresponding to viscous laminar flows. As noted in earlier work[1-3], this renders the flow fully viscous so that the boundary layer regions and core flow regions are indistinguishable. As a consequence, the presence of bounding walls in an internal flow is pervasive and affects the entire flow field. This has been demonstrated in recent work[4], where differences between 2-D and 3-D DSMC

results for the same geometry have been highlighted.

The focus of this paper is on studying flow characteristics in the transition regime in micronozzles using the Direct Simulation Monte Carlo (DSMC) method, with particular emphasis on the effects of the bounding walls on shock structure. Implications on the utility of the Navier-Stokes equations in this flow regime are also briefly addressed, and are shown to depend strongly on the viscosity used. The following section (Section II) describes the DSMC method used for simulating transition flows. The specific geometry and flow conditions studied in this work are described in Section III, and results are given for cases where collisions between the atoms of the gas and the bounding walls are diffuse and specular, respectively. The utility of numerical solution of the compressible Navier-Stokes equations in this flow regime is briefly addressed in Section IV, followed by a summary and conclusions in Section V.

II. The Direct Simulation Monte Carlo Method

The DSMC method used here to simulate transition flow in a micronozzle is based on the NTC method of G.A. Bird [5]. The essential property of the DSMC algorithm is that it mimics the physics contained in the Boltzmann Equation. The distribution function, $f(\vec{C}, \vec{r}, t)$, of molecular velocities at a point in space and an instant of time (\vec{r}, t) , along with molecular collision cross sections, determines the probability per unit time for molecules to undergo collisions near the point (\vec{r}, t) . The Boltzmann equation describes the time evolution of $f(\vec{C}, \vec{r}, t)$ in the presence of collisions.

In the DSMC technique, the flow field of interest is filled with molecules with a prescribed initial distribution of velocities. This can be done in many ways, and is ultimately immaterial when steady-state solutions are sought. Next, time is advanced forward in discrete steps, Δt , with $\Delta t < \sim (1/3)(\bar{\lambda}/\bar{C})$, so that a molecule undergoes a collision every three or more time steps, on average. In other words, less than one-third of all the molecules present in the flow undergo a collision during each time step. During each time step, molecules are advanced forward in position by an amount, $\vec{C}(\Delta t)$, and interact with walls and boundaries as they are encountered. Decoupled from their motion, molecules undergo collisions during each time step with other surrounding molecules according to the probabilities set forth by kinetic theory. Thus, DSMC may be viewed as a molecular dynamics simulation where molecular interactions are carried out probabilistically according to kinetic theory rather than by integrating equations of motion (i.e., $\vec{F} = m\vec{a}$). Equivalently, DSMC may be regarded as a rather robust way of obtaining solutions to the Boltzmann equation, since in principle (although computationally intensive) smooth microscopic distributions of any desired quantity may be obtained for virtually any flow geometry, wall interaction model, or boundary condition of interest.

The only important distinction to be made between Molecular Dynamics and DSMC is that in the latter, a “molecule”, which is referred to as a simulated molecule, really represents some large number, $\sim 10^{12}$, of real molecules. Such an approximate representation may be easily justified. In gas flows that are described well by kinetic theory, there are typically a large number of real molecules all possessing the same

microscopic properties. For a 2D flow with unit width (1 m), the number of real molecules with similar properties scales as $\sim \bar{\lambda}^{-2} (1\text{m})n \sim (10^{-4}\text{m})^2(1\text{m})(10^{22}\text{m}^{-3}) = 10^{14}$, where the values for $\bar{\lambda}$ and n are representative for the geometry and flow conditions considered in this paper.

The computational domain is divided into a non-uniform grid resulting in a network of cells, as shown in Fig. 2. Selection of collision partners and averaging of microscopic quantities is performed within the cells formed by the grid, which should have dimensions no greater than $\sim (1/3)\bar{\lambda}$. Physically, no flow properties can change over a distance of less than $\sim \bar{\lambda}$. Hence, it is ensured that gradients in the flow field are captured correctly. Of equal importance is that each cell contain enough simulated molecules (typically no less than 15) to allow many possibilities for collision pairs so as to yield physically correct solutions. Checks are made to ensure that these numerical approximations are justified by changing the number of simulated molecules and then calculating the changes in some flow field properties, such as mass flow rate or maximum Mach number. These changes will be negligibly small relative to the change in the number of simulated molecules, when enough simulated molecules are present.

The computational domain is divided into a 250 x 50 cell Cartesian grid, giving cell dimensions ranging from 2.27×10^{-5} m to 4.53×10^{-5} m in the axial direction and 1×10^{-5} m to 7×10^{-5} m in the transverse direction. Each cell is further subdivided into a 3 x 3 array of sub-cells in order to choose collision partners in as close proximity as possible. Between 10 (at the throat) and 25 (at the inlet) simulated Argon atoms are used per cell, with most of the

flow field in the diverging part of the micronozzle containing 15-18 simulated atoms per cell. Further, each simulated atom represents 10^{12} real atoms (assuming a flow width of 1 m).

The simulation evolves starting from an initial condition. Initially, at time zero, the nozzle is empty, that is, entirely void of any simulated atoms. The first stage of the simulation involves initiation of flow from a simulated upstream reservoir. Atoms are introduced at the inlet boundary according to the properties of the upstream reservoir, $T_o = 298$ K, $P_o = 1$ Torr. In other words, the simulated atoms introduced are chosen by sampling from the Maxwell-Boltzmann distribution function of a static gas at 298 K and 1 Torr. The number of particles to be introduced is obtained from the random thermal flux across the inlet plane over the time interval Δt ,

$$\Delta N = \frac{1}{4} n_o \left(\frac{8kT_o}{\pi m} \right)^{1/2} A_{\text{inlet}}(\Delta t). \quad \text{Next,}$$

positions (transverse locations along the inlet plane) are assigned for these particles using uniformly random numbers. This is followed by assigning C_x and C_y components of absolute velocity according to probabilities $\wp(C_x) \propto C_x e^{(-mC_x^2/2kT_o)}$ and $\wp(C_y) \propto e^{(-mC_y^2/2kT_o)}$, respectively. These atoms are then given axial displacements according to $C_x(\Delta t)$. These particles are then sorted according to their locations and placed into cells and sub-cells. Next, collisions are computed cell by cell, choosing collision partners within sub-cells or nearby sub-cells. These collisions result in new velocities for each simulated particle, which are deterministically computed to conserve momentum and energy after impact parameters have been selected randomly. The number of potential collisions per cell is given by:

$$\Delta N_C = (N_C^2/2)F_N(\pi d^2(C_{rel})_{MAX}\Delta t/V_C)$$

where N_C is the number of simulated molecules in the cell, V_C is the cell volume, $F_N = 10^{12}$ is the number of real molecules represented by each simulated molecule, and $(C_{rel})_{MAX}$ is any number larger than the maximum relative speed between molecules in a cell. Each potential collision is then accepted with probability, $C_{rel}/(C_{rel})_{MAX}$, where C_{rel} is the relative speed between the two molecules selected for a potential collision. This results in an average total number of collisions per cell of $\Delta N_C(\overline{C_{rel}}/(C_{rel})_{MAX})$. This mimics the collision probability per pair of molecules located within a volume V_C , which is established by kinetic theory as $\pi d^2 C_{rel} \Delta t / V_C$, since there are $(F_N N_C)^2 / 2$ pairs of real molecules per cell and each collision represents F_N real molecule collisions[5]. The new post-collision velocities are then used to advance the particles during the next time step. This procedure is repeated until the nozzle is filled with particles. The particles then begin to exit the nozzle downstream into vacuum, with no particles entering the micronozzle at the exit plane. This is analogous to the implicit extrapolation boundary conditions used at the exit plane in CFD continuum simulations of supersonic flows in nozzles. The time marching and particle moving operations continue until a steady supersonic flow ($M \sim 2-4$) is reached in the diverging portion of the nozzle.

One computational artifact should be addressed. Although the upstream reservoir is given the properties of $P_0 = 1$ torr and $T_0 = 298$ K, the value of total pressure just inside the nozzle inlet is less than 1 torr. In fact, for the specular wall, $(P_0)_{interior} = 0.8$ torr, while for the diffuse wall $(P_0)_{interior} = 0.9$ torr. The reason for this drop in total pressure

across the inlet boundary is that w , u , p , and T are discontinuous there. In other words, $w=0$ for the upstream reservoir, while $w \approx 60$ m/s $\neq 0$ immediately inside the nozzle inlet. These discontinuities are sources of irreversibility and therefore drop the total pressure. It should be emphasized, however, that in no way can this affect the flowfield downstream of the throat other than the effect of simply having an effectively lower pressure upstream reservoir. This is because the flow is choked, with supersonic flow downstream of the throat.

Once steady supersonic flow is attained in the nozzle, shocks can be produced by raising the back pressure along the exit plane. Just as in continuum simulations, all that is required to uniquely specify the flow field is an exit pressure, P_{exit} . However, unlike CFD simulations, pressure is not a molecular quantity but one that arises after averaging over molecular quantities. It is important to mention at the outset that a value of P_{exit} higher than the desired value must be initially prescribed in order to initiate change in the flow field inside the micronozzle. As the exit plane velocity decreases, P_{exit} can then be relaxed to the desired value. This back pressure P_{exit} is established by having a simulated downstream reservoir. At a given time level t , all flow quantities (u , w , n , P , and T) are known within each cell, albeit with significant statistical scatter. This information is used to obtain all the quantities except P and n in the downstream reservoir immediately beyond the exit plane, by averaging the relevant quantities (T , u , and w) over 10 cells lying 5-10 cells upstream of the exit plane. Further, the downstream reservoir is updated every 10 time steps in order to respond to the changing flow field within the micronozzle that its presence causes. It should be noted that these 5-10 last cells are skipped during

averaging to avoid the problem of the newly added molecules, which have a negative stream-wise component of velocity, dominating the averaging initially, resulting in an unstable downstream reservoir susceptible to positive feedback effects. The averaging consists of a fourth-order polynomial fit over the transverse direction for each quantity. The pressure in the downstream reservoir is fixed at a value of P_{exit} in order to obtain solutions where there are shocks present in the diverging portion of the nozzle. Specification of this back pressure, which is higher than the corresponding values in the interior of the nozzle, results in a net flux of simulated atoms into the flow field at the exit plane. A transient state ensues where the flow inside the nozzle must adjust for the flux of atoms that are thus introduced at the exit plane. Eventually, a steady-state is reached when the increased number of atoms in the diverging portion of the nozzle results in enough atoms exiting the simulation at each time step to balance the atoms entering at the inlet. In this final state, the profiles of T , u , v , n , and P in the downstream reservoir are identical to those just inside the nozzle. This condition is necessary in order for the steady state to be physically correct, i.e. the flow properties must be continuous across the exit plane.

At the centerline, symmetry boundary conditions are used. If a molecule crosses the centerline, its transverse position coordinate (y) and velocity component (u) are reversed. At the bounding walls, specular and thermally insulated diffuse wall interactions have been employed. If a molecule is displaced outside the domain during a move, the exact position of the wall encounter is calculated. Thereafter, the rule for altering the velocity is chosen based on the type of wall. The specular wall is simulated by reversing the component of

velocity normal to the wall, while maintaining the parallel component. During an encounter with a thermally insulated wall, the total kinetic energy of the molecule is conserved. This is implemented by separating the total kinetic energy of the molecule into two parts, one due to velocity normal to the wall, and the other due to velocity parallel to the wall. The normal component of the velocity of a particle reflected from the wall is sampled from

$$\wp(C_n^{(r)}) = \frac{2C_n^{(r)}}{C^{(i)}} \text{ for } C_n^{(r)} \in [0, C^{(i)}], \text{ where}$$

$C_n^{(r)}$ is the normal component of the reflected velocity in the x-y plane, $C^{(i)}$ is the incident speed. The tangential component of the reflected velocity, $C_t^{(r)} = \left([C^{(i)}]^2 - [C_n^{(r)}]^2 \right)^{1/2}$, has two components, one in the x-y plane, and another in the z direction. The z-component of $C_t^{(r)}$ is given by $C_t^{(r)} \sin(\xi)$ where ξ is a random number between 0 and 2π . The component of $C_t^{(r)}$ in the x-y plane is then obtained from $C_t^{(r)} \cos(\xi)$. These distributions for the reflected velocity are chosen so that the resulting partitioning of the reflected kinetic energy mimics a locally constant temperature wall. It can readily be seen from the given reflected velocity distributions that the average tangential velocity of a reflected molecule is zero, analogous to the no-slip wall boundary condition used in continuum simulations.

III. Results of DSMC Calculations for Transition Flow in the Micronozzle

The geometry considered in this work is shown in Fig. 1. It is planar (xy) with unit width (1 m) in the third dimension. The micronozzle is 8 mm long, comprising a 2 mm converging portion and 6 mm

diverging portion. Other dimensions are provided in Fig. 1. The area ratios (relative to the throat) at the inlet and exit are 3 and 7 respectively. Although the recent work of ref.[4] has shown the three-dimensional nature of such micronozzle flows, we restrict our attention to 2-D calculations due to limited computational resources. Our aim is to study the case of transition flows in micronozzles, where viscous effects begin to dominate. Operating conditions at the plenum ($P_o=0.8-0.9$ Torr, and $T_o=298$ K) are chosen so as to ensure an interesting range of Knudsen numbers based on the transverse throat dimension of 1 mm, as well as those based on the local transverse length scale[6]. A standing shock can be produced midway in the diverging portion of this nozzle by maintaining the back pressure at 0.2 Torr. We are specifically interested here in the structure of such shocks produced in the micronozzle, especially since the DSMC calculations admit a variety of gas-wall interactions ranging from diffuse walls (corresponding to the no-slip condition in the continuum case) to specular walls (maximum slip case). These two extremes bracket realistic gas-wall interactions and enable evaluation of the influence of the bounding surfaces on the transition flow.

The gas considered is Argon. In the DSMC simulations, a hard-sphere model is used for describing the collisional interactions between atoms of the gas. Results are presented for the case of diffuse walls and specular walls. Diffuse walls are those where the collisional interactions between the atoms and the walls are such that the atoms are reflected back into the flow in random directions, with an average tangential velocity equal to that of the wall, i.e. zero. This case corresponds to the no-slip walls typically encountered in continuum flows. Specular walls are those where the incident atoms are reflected back

into the flow field conserving their kinetic energies, with the component of incident velocity normal to the wall reversed upon reflection. This case corresponds to that of perfect slip at the walls, where the average velocity of the atoms at the walls is different from that of the wall itself, i.e. not zero. DSMC results are presented for the specular wall case first, followed by results for the diffuse walls.

Figures 3 through 5 show contour plots of the Mach number, Temperature, and Pressure. As can be seen from these contour plots, a shock clearly exists at $x = 4.5-6$ mm in the diverging portion of the nozzle. Figures 3-5 show the characteristic features of decrease in Mach number from supersonic to subsonic values across the shock, and increase in temperature and pressure across the shock, usually observed in shock waves in continuum flows. These characteristics are also evident in the centerline profiles of M , T , P , and w (streamwise or axial component of velocity), shown in Figs. 6-9, except that the shock thickness is over a millimeter. The shock is mostly planar with slight curvature and extends all the way to the bounding wall. The maximum Mach number of ~ 2.2 is reached at a location of ~ 4 mm downstream from the inlet. Figure 10 shows a contour plot of the local Knudsen number (defined as $Kn(x) = \bar{\lambda}/y_w(x)$, where $y_w(x)$ is the profile of the micronozzle wall), and it can be seen that in the vicinity of the shock, Kn is in the range of 0.06 to 0.16. Clearly, this range is in the transition regime and yet the shock appears on the scale of the micronozzle as shocks do in continuum flows.

The structure of the shock wave appears very different when the collisional interaction at the walls is diffuse while all other parameters ($P_o=0.9$ Torr, $T_o=298$ K,

and $P_{\text{exit}}=0.2$ Torr) are maintained. Figures 11 – 13 show contours of Mach number, Temperature, and Pressure for this case. In contrast to Figs. 3-5, it is evident that the flow is only weakly supersonic, reaching a maximum Mach number of only ~ 1.2 . Furthermore, there is no clearly discernible shock structure in this case of diffuse walls. Unlike the case with specular walls, the contours do not extend to the bounding walls. This is further apparent in Figs. 14 – 17, which show the centerline profiles of M, T, P, and w. It is apparent that there is no confined region where the supersonic flow is slowed to subsonic speeds through a shock. If this can indeed be referred to as a shock, then it is clearly spread out over the entire diverging portion of the micronozzle, with a thickness spanning 3 or 4 millimeters. This can be understood to be due to the viscous interaction arising from the diffuse collisions between the gas atoms and the bounding walls. In fact, in the case of the diffuse walls, the entire flow-field is viscous. The deceleration of the weakly supersonic flow in the micronozzle is reminiscent of classical continuum Fanno flow where a supersonic flow can be decelerated to subsonic speeds under the action of friction, without a shock. In contrast, a well-defined shock structure exists in the case of specular walls. This strongly suggests that the choice of material for a given propellant for the micronozzle can strongly influence its performance characteristics. Alternatively, it may be possible to develop novel coatings tailored for specific gases such that the micronozzle performance in the transition flow regime can be enhanced. The behavior of realistic surfaces is likely to be bounded between the two cases of diffuse and specular walls considered here.

Figures 18 and 19 show contours of shear stress for the specular and diffuse

walls, respectively. As can be seen in these figures, the shear stresses for the two cases show marked differences. In the case with specular walls (see Fig. 18), the shear is small or zero at the bounding wall and undergoes a change in sign at the throat. In contrast, the shear stress is of the same sign at the bounding wall in the diffuse wall case as can be seen from Fig. 19. Moreover, the magnitude of the shear is significantly higher with diffuse walls compared to specular walls. In both cases, the magnitude of the shear is highest near the throat of the micronozzle. This is to be expected since that is the smallest dimension and the location where the majority of the flow turning takes place. These results may be understood in the following way. The shear stress is defined microscopically as $\tau_{xy} = -\rho \langle C'_x C'_y \rangle$, where $C'_x = C_x - w$ and $C'_y = C_y - u$, and the average is taken over all molecules in a cell and over time. A negative value of τ_{xy} results from a correlation of $C'_x > 0$ with $C'_y > 0$, which is brought about by $\partial w / \partial y < 0$ and/or $\partial u / \partial x < 0$. Similarly, a positive value of τ_{xy} results from $\partial w / \partial y > 0$ and/or $\partial u / \partial x > 0$. For the case of a specular wall, τ_{xy} changes from negative just before the throat to positive immediately after the throat. This is brought about almost solely by flow turning and positive acceleration, which causes $\partial u / \partial x < 0$ before the throat and $\partial u / \partial x > 0$ after the throat. Although $\partial w / \partial y < 0$ due to the cusp at the throat, it is smaller in magnitude than $\partial u / \partial x$ in either case. For the case of the diffuse wall, the flow field is fully viscous with $\tau_{xy} < 0$

everywhere. This is because $\partial w/\partial y < 0$ is the dominant contribution to τ_{xy} due to the near zero velocity at the wall. Flow turning is more gradual for the diffuse wall (due to viscous effects), making $\partial u/\partial x$ small compared to $\partial w/\partial y$, and thus τ_{xy} negative everywhere. This suggests once again that surface modification of the bounding walls of the micronozzle either by application of a suitable coating or by choice of the wall material can have a significant impact on the performance and flow characteristics of microthrusters.

In this section results of DSMC simulations for transition flow ($0.03 < \text{local Kn} < 0.22$) with shocks has been examined. It is found that shock structure is profoundly influenced by the nature of the interaction between the gas atoms and the bounding walls. For specular walls, a discernible shock is observed even in transition flow with a shock thickness of approximately 1.5 millimeters (or $\sim 4-5 \bar{\lambda}$'s). In contrast, the shock is spread out over the entire diverging portion of the micronozzle for a diffuse wall with a thickness of 3-4 mm and the extremely viscous nature of the flow is all too apparent in this case. In the following section, the present problem is briefly analyzed using numerical solution of the compressible Navier-Stokes equations with no-slip walls.

IV. Solution of the Compressible Navier-Stokes Equations for Transition Flow in the Micronozzle

Although the focus of this paper is on transition flow and applicability of the Navier-Stokes equations in this regime is questionable, it is nevertheless instructive to explore the behavior of continuum solutions in the near-transition regime. In this section,

we briefly describe the behavior of the flow as predicted by the compressible Navier-Stokes equations for the same geometry, with no-slip conditions applied at the walls. The compressible Navier Stokes equations together with conservation of energy, were solved numerically using the finite-difference Linearized Block Implicit (LBI) method[7]. This method is described in detail elsewhere[8], and therefore will not be described here.

A 260 x 50 uniform grid is used for the results presented here, with a minimum amount of numerical dissipation required for stability of the time-marching scheme. As in the DSMC case, P_o , and T_o are prescribed at the inlet boundary. The axial and transverse components of velocity are implicitly extrapolated. At the exit plane, the axial and transverse components of velocity are implicitly extrapolated. The static temperature is extrapolated as well. In order to obtain shocks in the diverging portion of the geometry, a value of the exit pressure is prescribed. Initial profiles are prescribed for ρ , u , w , and T , and the governing equations are time-marched until steady state is reached.

The continuum calculations use the approximate viscosity obtained from the Chapman-Enskog solution of the Boltzmann equation for collisions between hard spheres[5]:

$$\mu = \frac{5}{16} \frac{m}{d^2} \sqrt{\frac{RT}{\pi}} \quad (1)$$

This expression is strictly valid in the collision-dominated limit and while it captures the correct variation of viscosity with temperature, it is independent of the mean free path. Consequently, use of equation (1) with the Navier-Stokes equations limits its applicability to the collision-dominated regime of very low Knudsen numbers ($\text{Kn} < 10^{-3}$)[16].

For $P_o=1$ Torr and $T_o=298$ K, it was found that for viscosities given by equation (1), the flow was subsonic ($M<1$) throughout the domain (i.e., it was not choked). A solution yielding supersonic flow in the diverging portion of the micronozzle could be found only when P_o was raised to 1.8 Torr with $T_o=298$ K. For a $P_{\text{exit}}=0.2$ Torr, the maximum centerline Mach number matched that value obtained in the DSMC calculations, as can be seen from Fig. 20 and Fig. 14. However, downstream of this location where the Mach number attains a maximum, the two solutions are *very* different for the *same* downstream boundary conditions ($P_{\text{exit}}=0.2$ Torr). The Navier-Stokes solution with no-slip walls and $P_o=1.8$ Torr, predicts a weakly supersonic flow in the diverging portion of the micronozzle, whereas the DSMC solution with diffuse walls predicts the presence of a thick shock forcing the flow in the diverging portion to be largely subsonic. Figures 21-23 show profiles of the temperature, pressure, and streamwise (axial) component of velocity along the centerline for this case. Comparing these Figs. 20-23 with Figs. 14-17, it can be seen that while the Navier-Stokes results for $T(x)$ and $w(x)$ for $P_o=1.8$ Torr are quantitatively different from the corresponding DSMC results for $P_o=1$ Torr with diffuse walls, they are *qualitatively similar*. It can be seen that as a result of increased wall shear and viscous effects in the flow, both Navier-Stokes and DSMC solutions exhibit significant heating by viscous dissipation. Despite the quantitative disagreement between the two, an even more striking difference is the fact that the DSMC results correctly predict a shock spread out over the diverging portion of the micronozzle, while the Navier-Stokes results predict a supersonic (albeit decelerating) flow.

The dramatic increase in viscous action as the transition region is approached, can be seen in Figs. 20-23 where P_o was varied from 7.5 Torr to 1.8 Torr in the Navier-Stokes calculations. As can be seen from these figures, the flow is an accelerating supersonic flow usually observed in collision-dominated regimes. However, as P_o approaches 1.8 Torr, the effects of increased viscous action relative to flow inertia can be clearly seen. The Mach number while greater than 1 for $P_o=1.8$ Torr, exhibits a local maximum and decreases downstream. The temperature profile along the centerline shows a dramatic difference in Fig. 23 for the $P_o=7.5$ Torr and $P_o=1.8$ Torr cases. There is monotonic decrease in temperature for $P_o=7.5$ Torr, exactly as would be expected for a flow smoothly accelerating from subsonic to supersonic speeds in a converging-diverging nozzle. In contrast, the centerline temperature for $P_o=1.8$ Torr exhibits non-monotonic behavior, with an increasing temperature arising from viscous dissipation in the diverging portion of the micronozzle. This is qualitatively similar to the DSMC result (see Fig. 15).

Based on the continuum results presented here for the geometry described in Section III, it would be tempting to conclude that the Navier-Stokes equations are invalid for the transition flow considered here. However, that would be an erroneous conclusion because it must be borne in mind that it is not the equations themselves that are limited in applicability but the constitutive equation (1) for the viscosity obtained from the Chapman-Enskog solution of the Boltzmann equation. The DSMC method could in principle be applied to prototypic Couette flows under a variety of conditions (temperature, strain rate, and mean free path or Knudsen number). The results from such a simulation could then be

expressed in a usable form for μ as a function of T , $\partial w/\partial y$, $\partial u/\partial x$, and $\bar{\lambda}$, replacing equation (1) for substitution in the Navier-Stokes equations. Such an approach would extend the Navier-Stokes equations from continuum through slip-flow into the transition regime, and would be a worthwhile pursuit for future work.

V. Summary & Conclusions

Supersonic flow of Argon through a converging-diverging micronozzle in the transition regime has been examined in this work, with particular emphasis on shock structure. The geometry has been chosen so as to yield Knudsen numbers based on the transverse dimension of the throat or local transverse dimension, in the transition regime ($0.03 < \text{local Kn} < 0.22$). Using the DSMC method, numerical solutions have been obtained for the limiting cases of diffuse walls and specular walls, for a total pressure of 1 Torr, total temperature of 298 K, and a prescribed exit pressure of 0.2 Torr. For pedagogical purposes, solutions to the compressible Navier-Stokes equations with no-slip walls and with the viscosity obtained from the Chapman-Enskog solution of the Boltzmann equation, are provided for the same geometry.

For the micronozzle geometry considered in this paper, DSMC calculations show that a discernible shock wave occurs in the diverging portion of the micronozzle when the collisional interaction between the gas atoms and the bounding walls is specular. However, for the same upstream and downstream conditions, diffuse walls yield a weakly supersonic flow with a shock wave spread out over most of the diverging portion. As expected, the flow is seen to be highly viscous.

Solutions to the Navier-Stokes equations with no-slip walls and a

Chapman-Enskog viscosity were explored for the same geometry. These predicted purely subsonic flow throughout the nozzle. Supersonic solutions could only be obtained for $P_o \geq 1.8$ Torr, and none of these solutions yielded a shock wave diffuse or otherwise in the diverging portion of the micronozzle. Although viscous effects were significant at the lower P_o in the neighborhood of 1.8 Torr, higher values of P_o near 7.5 Torr yielded flow smoothly accelerating from subsonic to supersonic speeds in the micronozzle. Moreover, the Navier-Stokes solution closest to the DSMC calculations were for $P_o=1.8$ Torr, and these were in *complete disagreement* with DSMC results. This discrepancy is due to the inadequacy of the Chapman-Enskog viscosity along with the higher Re associated with $P_o=1.8$ Torr rather than $P_o=0.9$ Torr, and not because of inapplicability of the compressible Navier-Stokes equations in the transition regime.

Of significance is the impact of the gas-wall interaction, as demonstrated in the DSMC results reported here. Although previous work [1-4] has reported changes in nozzle performance as a result of the gas-wall interactions, this work shows that shock structure can be substantially influenced and modified. As we have shown here, specular walls can produce distinct shock structure similar to that observed in internal continuum flows with shocks present. In contrast, diffuse walls render the whole flow domain viscous under the conditions considered here, and spread the shock over a substantial portion of the nozzle. This suggests that DSMC calculations for flow in micronozzles should include the nature of the material of the bounding wall and its associated interaction with colliding atoms or molecules of the gas. This also presents an opportunity for altering the performance of micronozzles and other micro-devices by

use of an appropriate coating tailored to the particular gas or fluid flow of interest.

Acknowledgements:

This work was supported in part by AFOSR grant F49620-00-1-0169.

References:

- [1] D. Zelesnik, M. M. Micci, and L. N. Long, "Direct Simulation Monte Carlo Model of Low Reynolds Number Nozzle Flows", **J. Propulsion & Power**, Vol. 10, No. 4, pp. 546-553, July-Aug. 1994.
- [2] E. S. Piekos & K. S. Breuer, "Numerical Modeling of Micromechanical Devices using the Direct Simulation Monte Carlo Method", **J. Fluids Eng.**, vol. 118, pp. 464-469, September 1996.
- [3] R. L. Bayt & K. S. Breuer, "Viscous Effects in Supersonic MEMS-Fabricated Micronozzles", Proc. 3rd ASME Microfluids Symposium, Anaheim, California, November 1998.
- [4] A. A. Alexeenko, S. F. Gimelshein, D. A. Levin, and R. J. Collins, "Numerical Modeling of Axisymmetric and Three-Dimensional Flows in MEMS Nozzles", paper AIAA-2000-3668 presented at the 36th AIAA/ASME/SAE/ASEE Joint Propulsion Conference and Exhibit, Huntsville, Alabama, July 16-19, 2000.
- [5] G. A. Bird, *Molecular Gas Dynamics and Direct Simulation of Rarefied Gas Flows*, Oxford Science Publication, 1994.
- [6] A. Beskok, G. Karniadakis, and W. Trimmer, "Rarefaction and Compressibility in Gas Microflows", **J. Fluids Eng. Trans. ASME**, Vol. 118, pp. 448-456, September 1996.
- [7] W. R. Briley, and H. McDonald, "Solution of the Multidimensional

Compressible Navier-Stokes Equations by a Generalized Implicit Method", **J. Comp. Phys.**, Vol. 24, 1977, pp. 372-397.

- [8] S. M. Aithal, V. V. Subramaniam, J. Pagan, and R. Richardson, "Numerical Model of a Transferred Plasma Arc", **J. Appl. Phys.**, Vol. 84, No. 7, pp. 1-12, October 1, 1998.

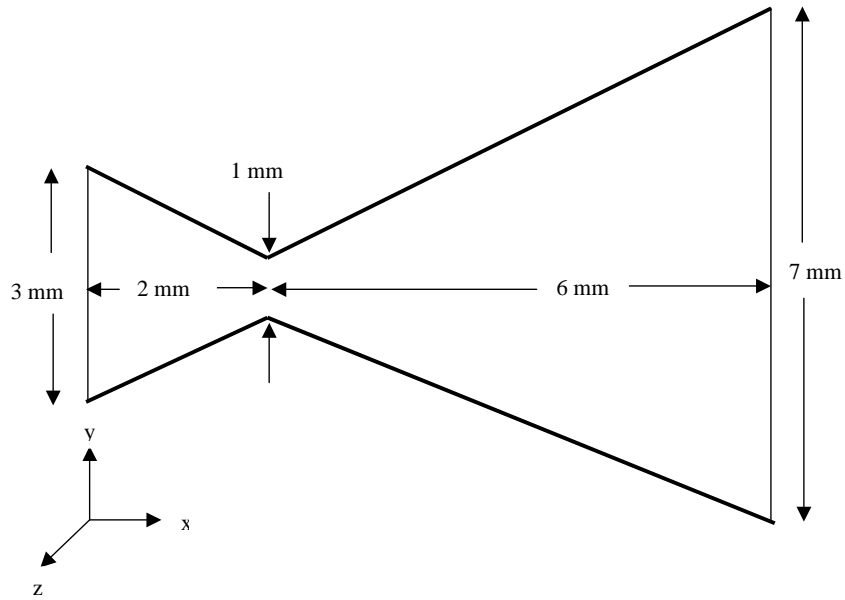


Fig. 1: Schematic of the micronozzle geometry studied in this work.

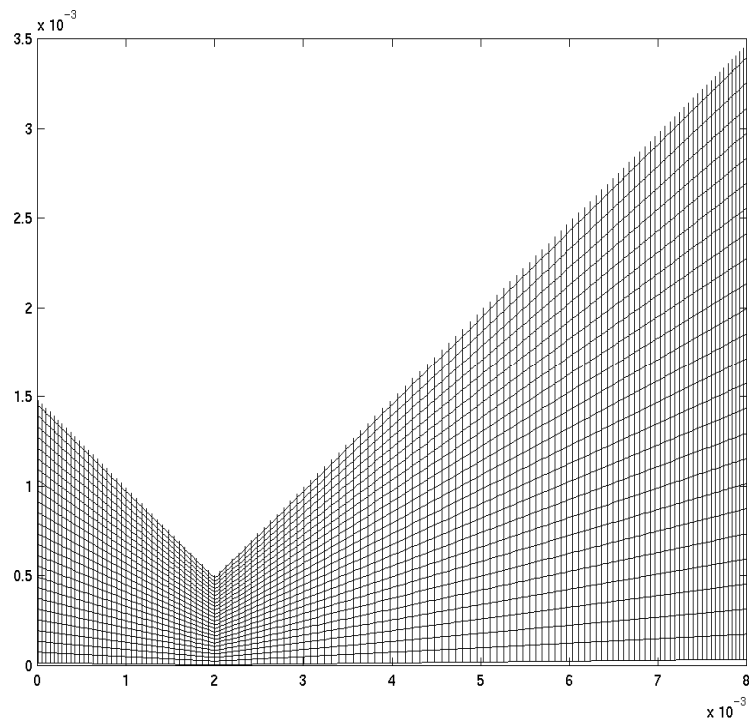


Fig. 2: Non-uniform grid used in the DSMC calculations. Only every other grid point is shown here for plotting purposes.

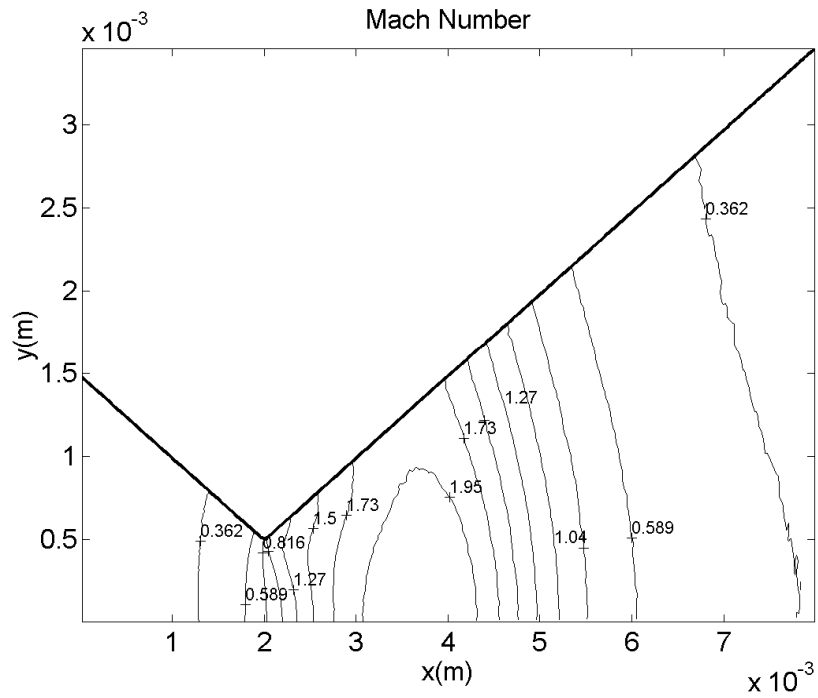


Fig. 3: Contours of Mach number are shown here from DSMC calculations for the specular wall case, with $P_0=1$ Torr, $T_0=298$ K, and $P_{\text{exit}}=0.2$ Torr.

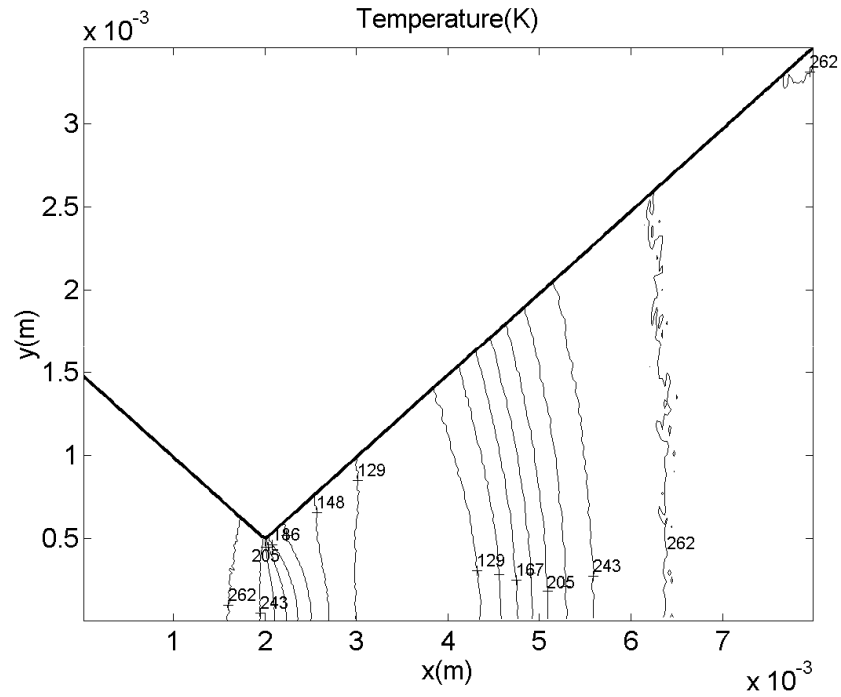


Fig. 4: Contours of temperature are shown here from DSMC calculations for the specular wall case, with $P_0=1$ Torr, $T_0=298$ K, and $P_{\text{exit}}=0.2$ Torr.

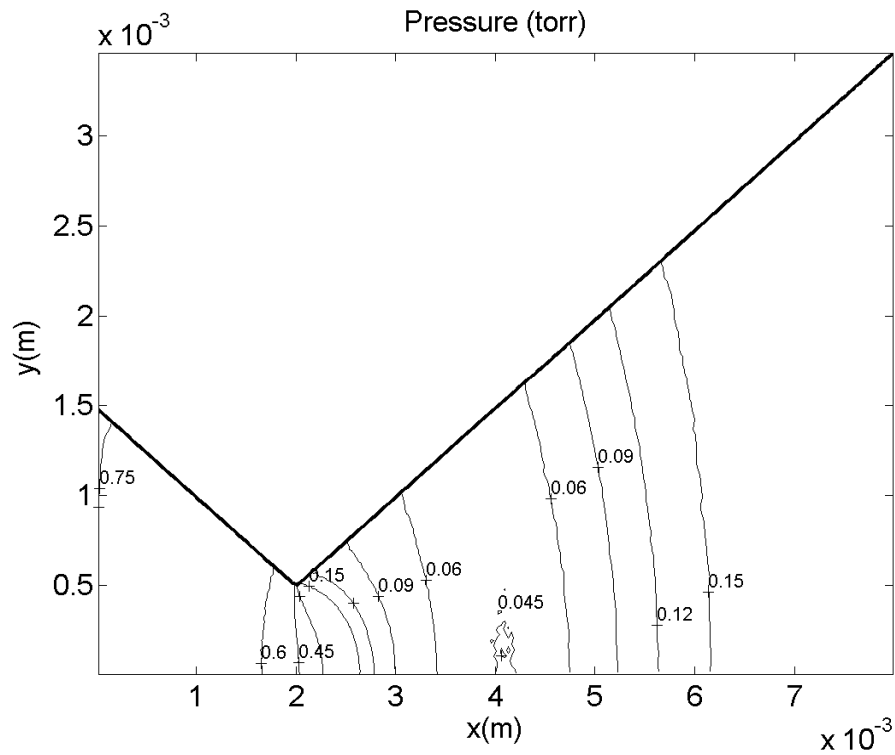


Fig. 5: Contours of pressure are shown here from DSMC calculations for the specular wall case, with $P_0=1$ Torr, $T_0=298$ K, and $P_{\text{exit}}=0.2$ Torr.

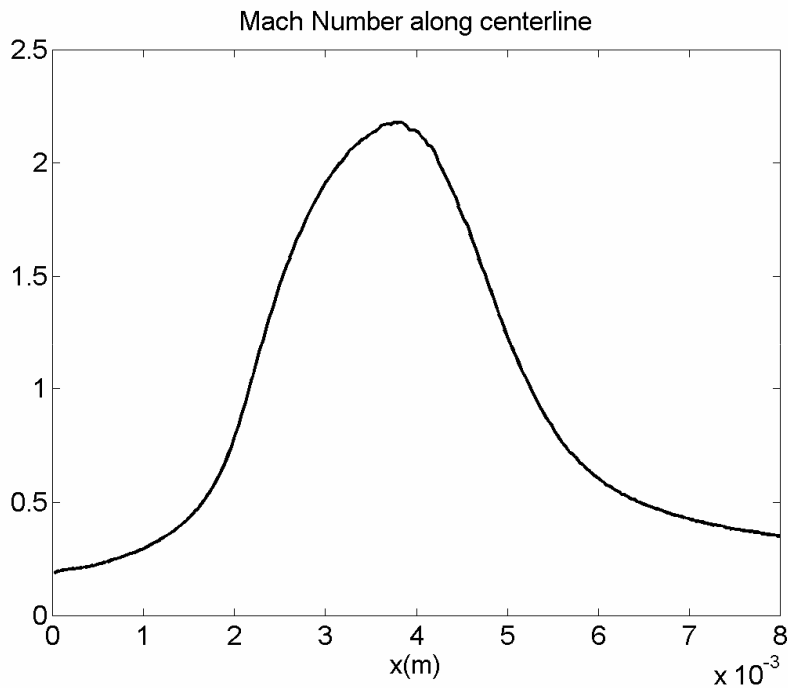


Fig. 6: Variation of Mach number along the centerline calculated from DSMC simulations is shown here for the specular wall case, with $P_0=1$ Torr, $T_0=298$ K, and $P_{\text{exit}}=0.2$ Torr.

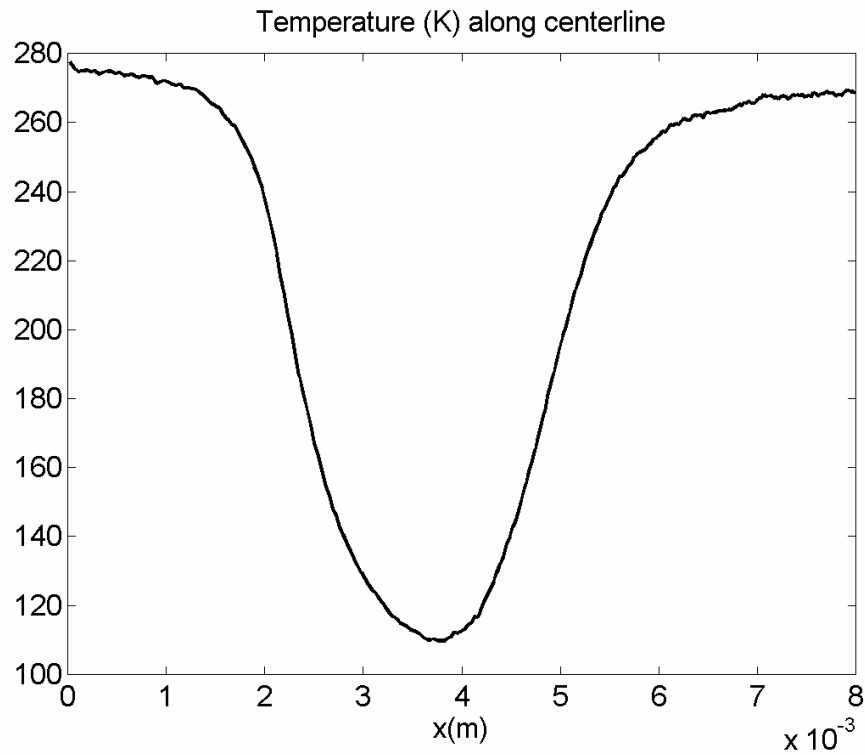


Fig. 7: Variation of temperature along the centerline calculated from DSMC simulations is shown here for the specular wall case, with $P_o=1$ Torr, $T_o=298$ K, and $P_{\text{exit}}=0.2$ Torr.

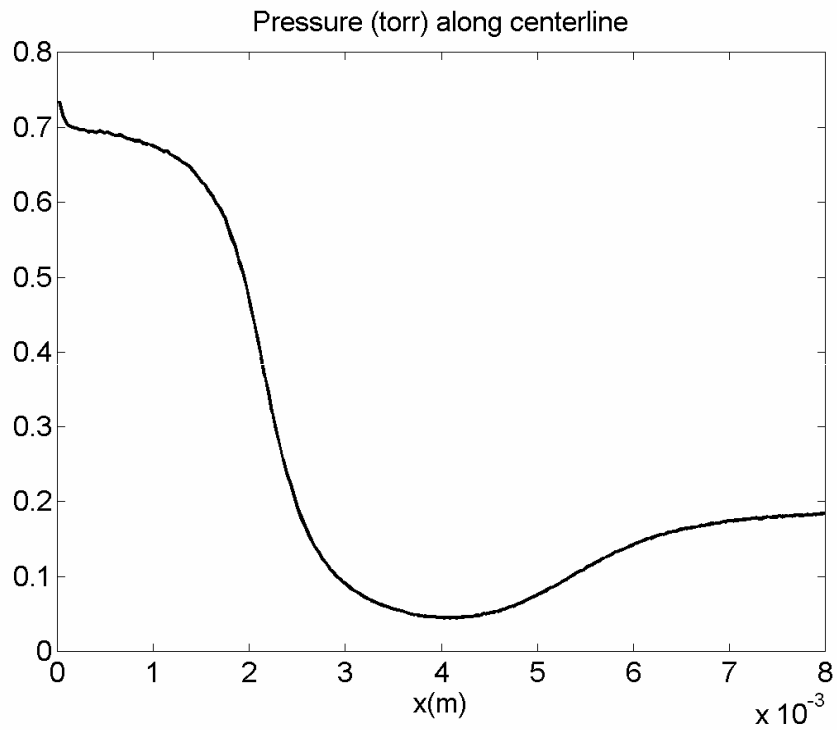


Fig. 8: Variation of pressure along the centerline calculated from DSMC simulations is shown here for the specular wall case, with $P_o=1$ Torr, $T_o=298$ K, and $P_{\text{exit}}=0.2$ Torr.

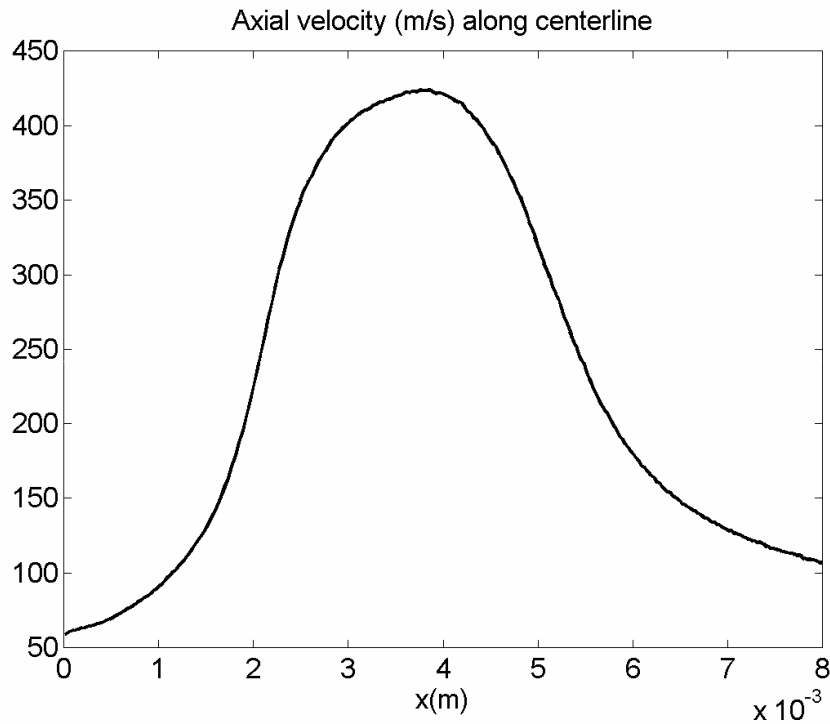


Fig. 9: Variation of streamwise (axial) component of velocity along the centerline calculated from DSMC simulations is shown here for the specular wall case, with $P_o=1$ Torr, $T_o=298$ K, and $P_{exit}=0.2$ Torr.

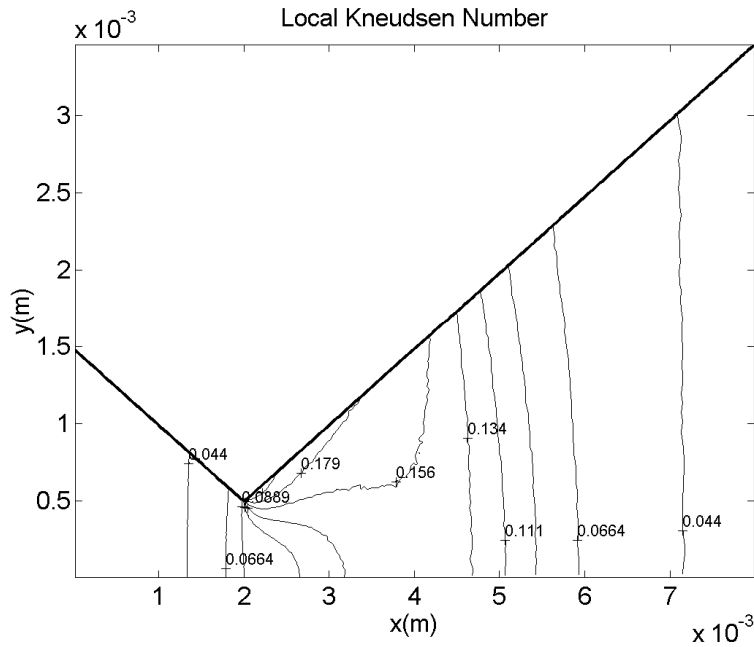


Fig. 10: Contours of Knudsen number ($Kn = \bar{\lambda}/y_w(x)$) based on the local transverse dimension of the bounding wall, are shown here from DSMC calculations for the specular wall case, with $P_o=1$ Torr, $T_o=298$ K, and $P_{exit}=0.2$ Torr.

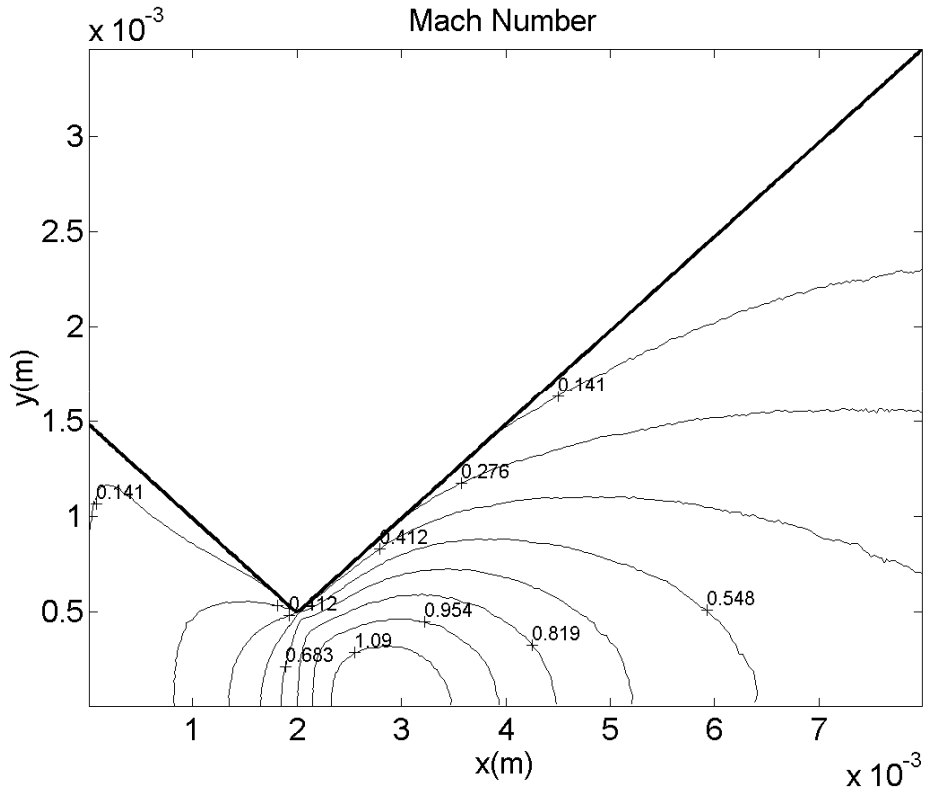


Fig. 11: Contours of Mach number are shown here from DSMC calculations for the diffuse wall case, with $P_o=1$ Torr, $T_o=298$ K, and $P_{exit}=0.2$ Torr.

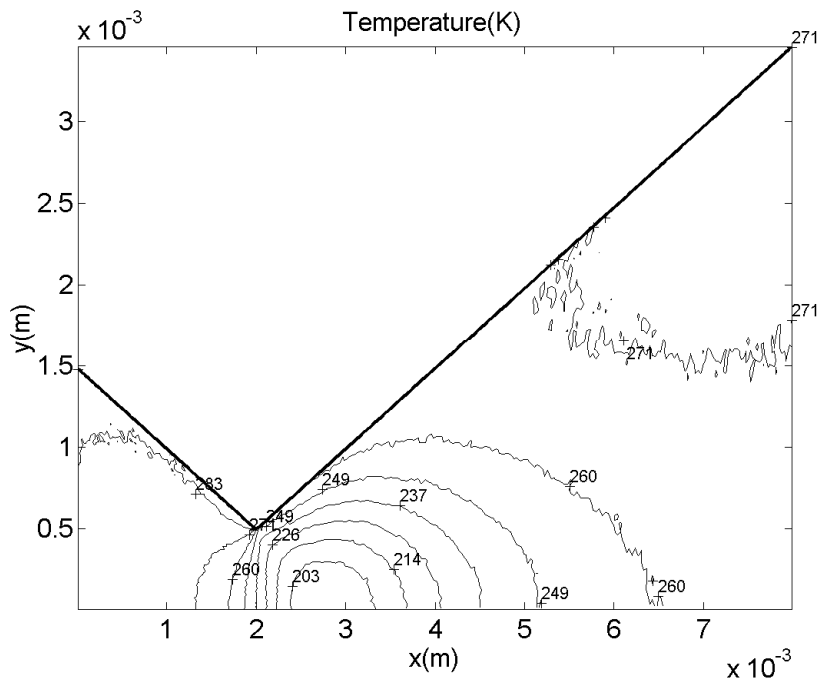


Fig. 12: Contours of temperature are shown here from DSMC calculations for the diffuse wall case, with $P_o=1$ Torr, $T_o=298$ K, and $P_{exit}=0.2$ Torr.

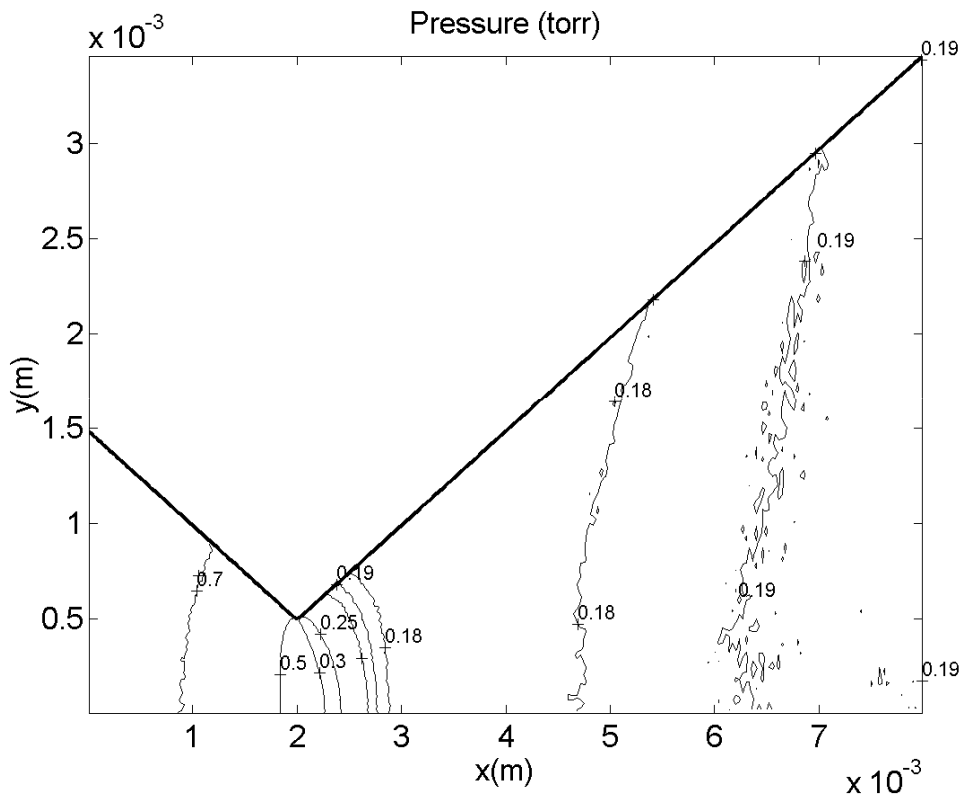


Fig. 13: Contours of pressure are shown here from DSMC calculations for the diffuse wall case, with $P_0=1$ Torr, $T_0=298$ K, and $P_{\text{exit}}=0.2$ Torr.

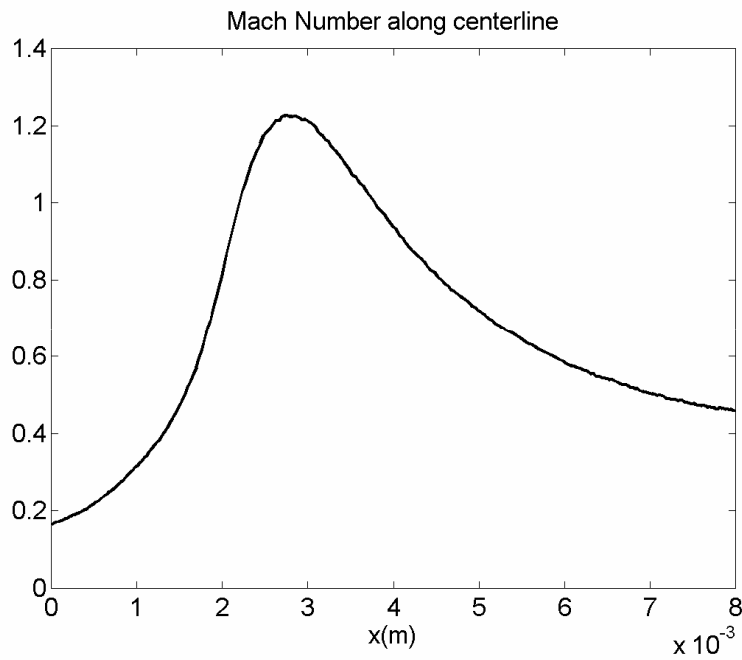


Fig. 14: Variation of Mach number along the centerline calculated from DSMC simulations is shown here for the diffuse wall case, with $P_0=1$ Torr, $T_0=298$ K, and $P_{\text{exit}}=0.2$ Torr.

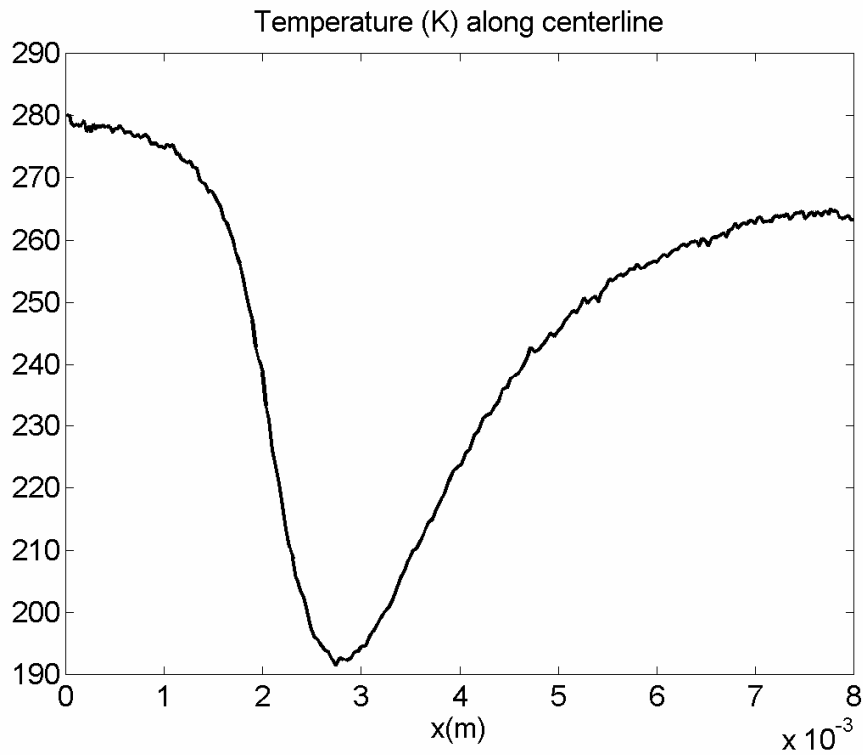


Fig. 15: Variation of temperature along the centerline calculated from DSMC simulations is shown here for the diffuse wall case, with $P_o=1$ Torr, $T_o=298$ K, and $P_{exit}=0.2$ Torr.

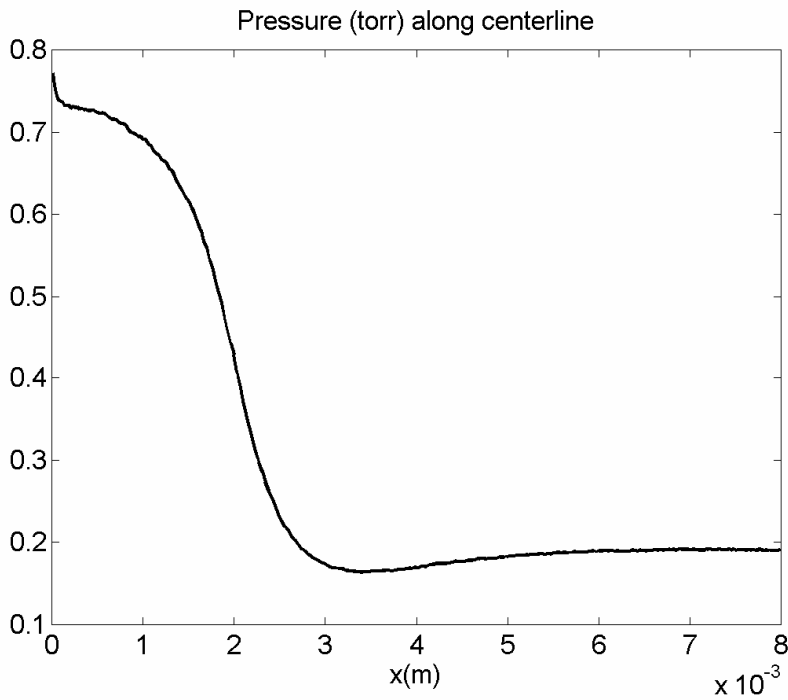


Fig. 16: Variation of pressure along the centerline calculated from DSMC simulations is shown here for the diffuse wall case, with $P_o=1$ Torr, $T_o=298$ K, and $P_{exit}=0.2$ Torr.

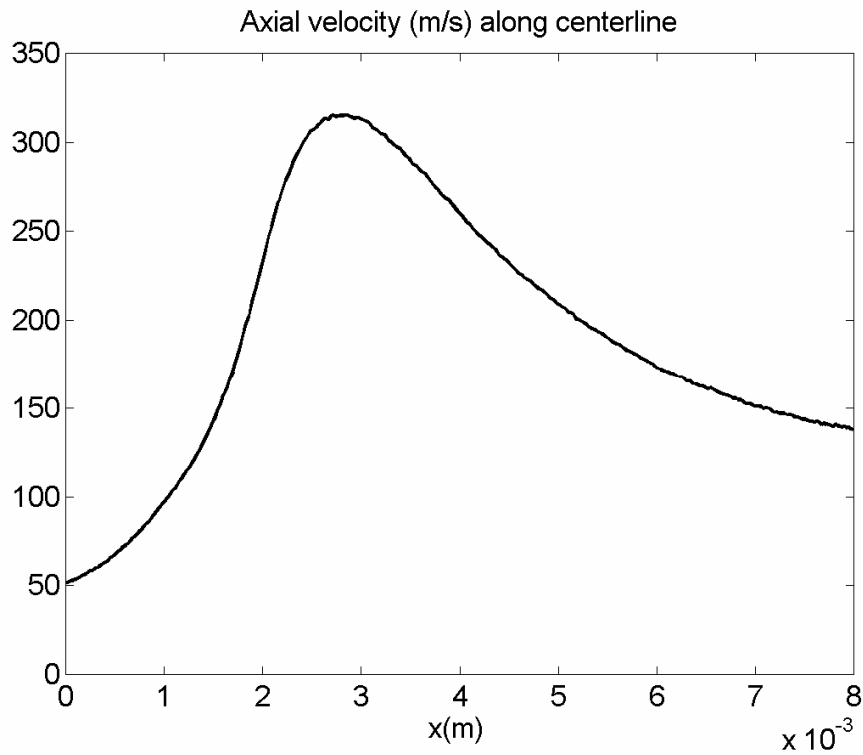


Fig. 17: Variation of streamwise (axial) component of velocity along the centerline calculated from DSMC simulations is shown here for the diffuse wall case, with $P_o=1$ Torr, $T_o=298$ K, and $P_{exit}=0.2$ Torr.

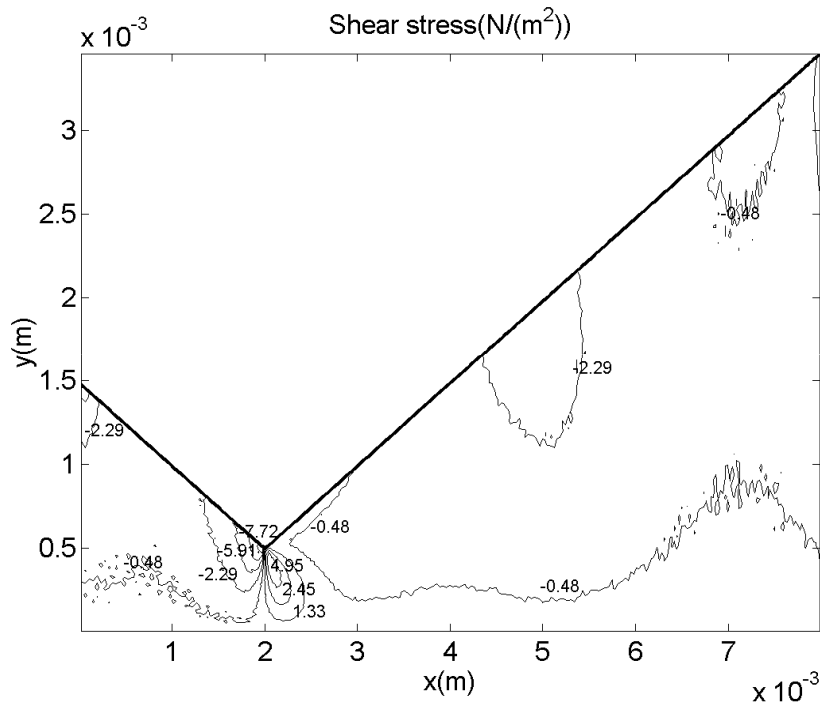


Fig. 18: Contours of shear stress are shown here from DSMC calculations for the specular wall case, with $P_o=1$ Torr, $T_o=298$ K, and $P_{exit}=0.2$ Torr.

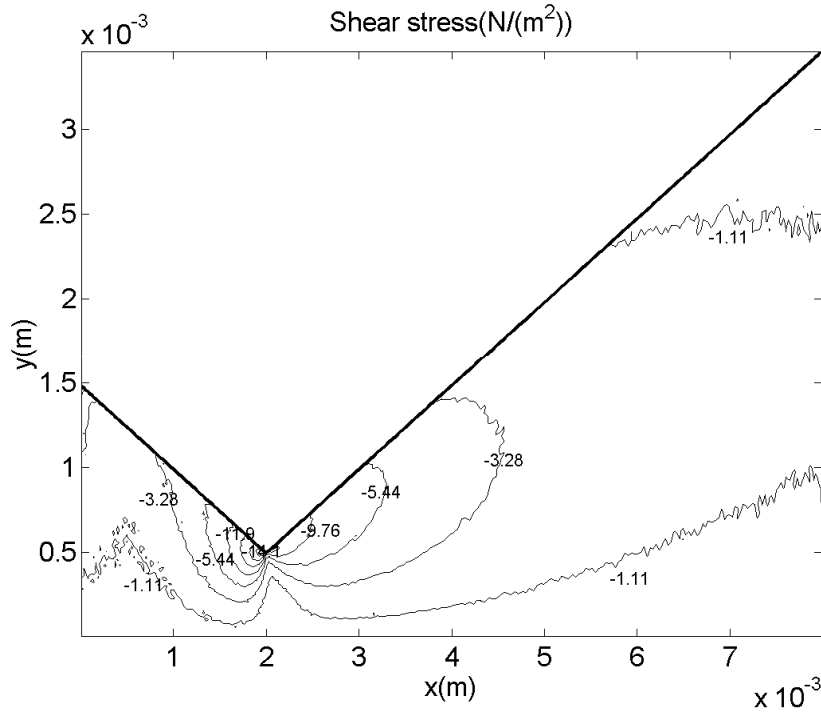


Fig. 19: Contours of shear stress are shown here from DSMC calculations for the diffuse wall case, with $P_0=1$ Torr, $T_0=298$ K, and $P_{\text{exit}}=0.2$ Torr.

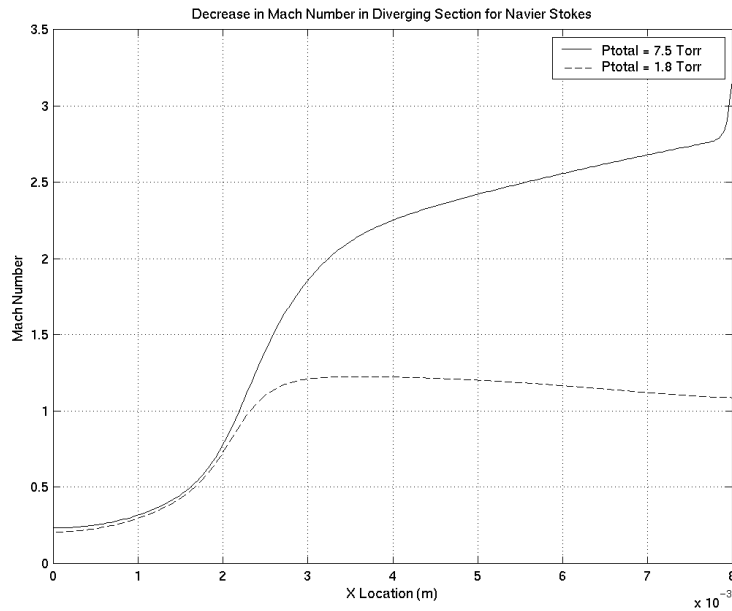


Fig. 20: Variation of Mach numbers along the centerline from numerical solution of the compressible Navier-Stokes equations are shown here, with $T_0=298$ K, $P_{\text{exit}}=0.2$ Torr, and for two values of P_0 : 1.8 Torr, and 7.5 Torr. Note the increasing influence of viscous effects as P_0 is reduced from 7.5 Torr to 1.8 Torr.

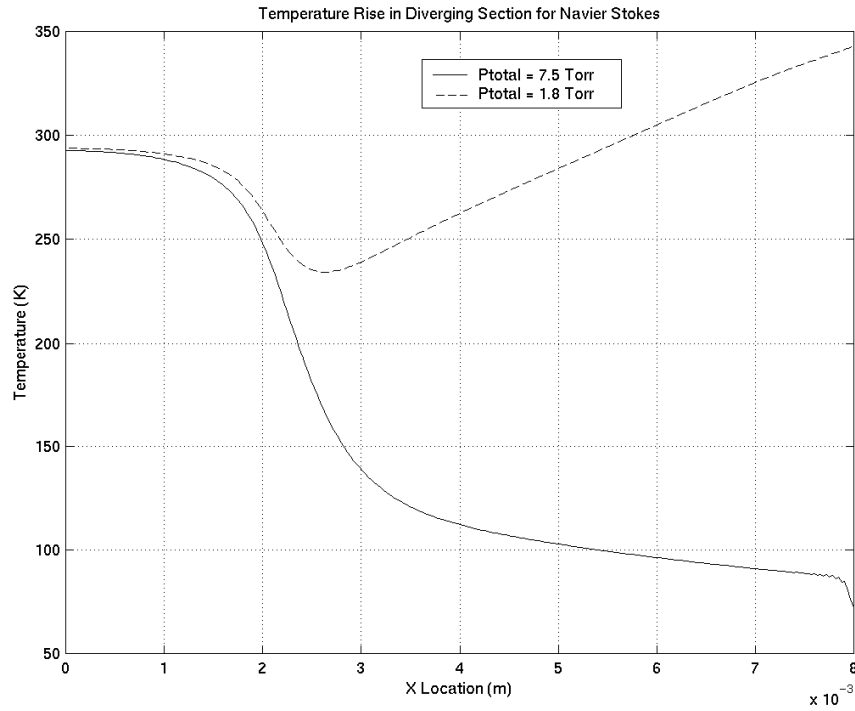


Fig. 21: Variation of temperatures along the centerline from numerical solution of the compressible Navier-Stokes equations are shown here, with $T_o=298$ K, $P_{exit}=0.2$ Torr, and for two values of P_o : 1.8 Torr, and 7.5 Torr. Note the increasing influence of viscous effects as P_o is reduced from 7.5 Torr to 1.8 Torr.

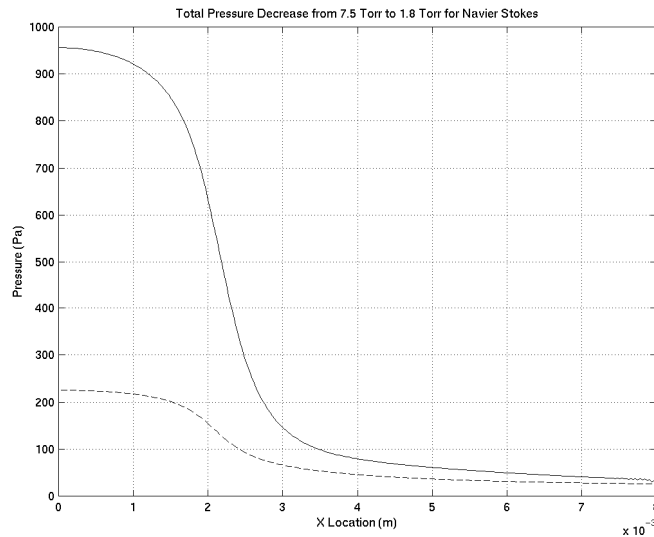


Fig. 22: Variation of pressures along the centerline from numerical solution of the compressible Navier-Stokes equations are shown here, with $T_o=298$ K, $P_{exit}=0.2$ Torr, and for two values of P_o : 1.8 Torr, and 7.5 Torr. Note the increasing influence of viscous effects as P_o is reduced from 7.5 Torr to 1.8 Torr.

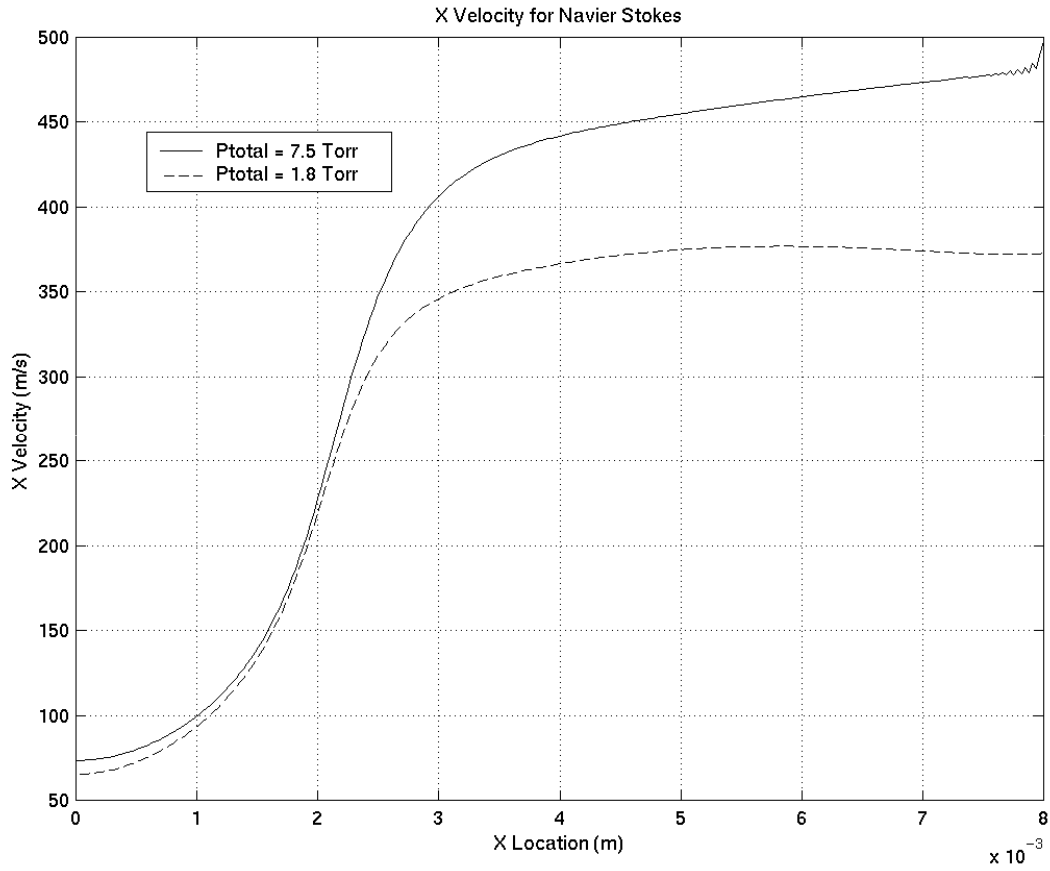


Fig. 23: Variation of streamwise (axial) components of velocity along the centerline from numerical solution of the compressible Navier-Stokes equations are shown here, with $T_o=298$ K, $P_{exit}=0.2$ Torr, and for two values of P_o : 1.8 Torr, and 7.5 Torr. Note the increasing influence of viscous effects as P_o is reduced from 7.5 Torr to 1.8 Torr.